

A COMPREHENSIVE FRAMEWORK FOR EARLY ASSESSMENT OF LUNG INJURY

Ahmed Soliman¹, Fahmi Khalifa², Ahmed Shaffie^{1,3}, Neal Dunlap⁴,
Brain Wang⁴, Adel Elmaghraby³, Georgy Gimel'farb⁵, Mohammed Ghazal^{1,6}, and Ayman El-Baz^{1*}

¹BioImaging Laboratory, Bioengineering Department, University of Louisville, Louisville, KY, USA.

²Electronics and Communication Engineering Department, Mansoura University, Mansoura, Egypt.

³Computer Engineering and Computer Science Department, University of Louisville, Louisville, KY, USA.

⁴Department of Radiation Oncology, University of Louisville, Louisville, KY, USA.

⁵Computer Engineering and Computer Science Department, University of Auckland, Auckland, New Zealand.

⁶Department of Electrical and Computer Engineering, Abu Dhabi University, Abu Dhabi, UAE

ABSTRACT

A novel framework for the detection of radiation-induced lung injury (RILI) from 4D computed tomography (CT) has been proposed. Our framework performs 4D-CT lung fields segmentation, deformable image registration (DIR), extraction of textural and functional features, and classification of lung voxels using deep 3D convolutional neural networks (CNN). The 4D-CT images segmentation extracts the lung fields inside the exhale phase using our multi-scale Gaussian adaptive shape prior technique followed by label propagation to other 4D-CT phases using a newly developed adaptive shape model. Then, the 4D-CT DIR locally aligns consecutive phases of the respiratory cycle using the 3D Laplace equation for finding voxel correspondences between the iso-surfaces for the fixed and moving lungs and generalized Gaussian Markov random field (GGMRF) as an anatomical consistency constraint. In addition to common lung functionality features, such as ventilation and elasticity, specific regional textural features are estimated by modeling the segmented images as samples of a novel 7th-order contrast-offset-invariant Markov-Gibbs random field (MGRF). Finally, a deep 3D CNN is applied to distinguish between the injured and normal lung tissues. 4D-CT datasets collected from 13 patients, who undergone the radiation therapy (RT), have been used in the evaluation of the proposed framework. The experimental results show the promise of our framework.

Index Terms—4D-CT, Lung Deformation, RILI, Lung segmentation

1. INTRODUCTION

The main side effect of radiation therapy (RT) for lung cancer patients is the development of lung Radiation-induced lung injury (RILI). Almost 40% of patients who undergone the RT developed lung injuries following treatment [1]. Lung injury can be acute radiation pneumonitis which always happens less than six months, or later, called lung fibrosis, which happens after six months [2]. Early detection of lung injury will help to improve management of the treatment and reverse the injury progression (see Fig. 1). Currently, global pulmonary function tests (PFT), such as spirometry, measure an airflow obstruction/restriction without providing regional lung function information. Alternatively, the lung functionality can be locally evaluated using nuclear imaging, e.g., SPECT ventilation and perfusion (V/Q) images. The acquisition of SPECT images is very expensive and uses relatively slow machines, and the images have too low spatial resolution. Relying on only the visual appearance, i.e., Hounsfield units (HU), leads to a late RILI detection that will make the treatment more difficult. As an alternative, detecting the early RILI development through monitoring lung functionality and lung texture changes could substantially improve the disease management. Four-dimensional computed tomog-

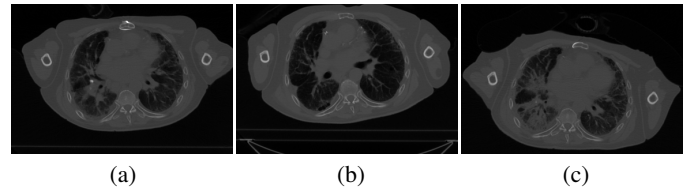


Fig. 1. Effect of radiation on lung tissues; three axial slices from Pre-treatment (a), 3 months (b), and 6 months (c) follow-up scans. Images are cropped from the same position to show the misalignment effects.

raphy (4D-CT) are acquired as part of routine care for lung cancer patients and have gained attention for assessing lung functionality as the derived ventilation maps provides high spatial resolution, faster acquisition, and no extra money or dose cost to the patient. Moreover, in addition to texture, many other functional features can be derived from the 4D-CT scans [3]. Latifi et al. [4] showed that the lung ventilation maps based on the 4D-CT correlate with 3D radiation dose distributions and suggested that these maps can be used in treatment planning to spare functional lung volumes. Reinhardt et al. [5] estimated local lung expansion from multiple respiratory CT images and showed that the Jacobian of the registration displacement field directly relates to a specific volume change. A quantitative study by Cunliffe et al. [6] measured lung reactions to the RT and assessed the radiation pneumonitis (RP) development by extracting intensity-based information to distinguish between the RP and non-RP patients. Douglas et al. [7] validated the use of 4D-CT ventilation maps through the comparison with pulmonary function tests (PFTs). The correlation coefficients for the comparison ranged from 0.63 – 0.72 with the best agreement between forced expiratory volume in 1 second (FEV1) and coefficient of variation (CoV). Sharifi et al [8] presented a prediction model for radiation-induced lung damage (RILD) by measuring only the lung tissue density changes per voxel. Hu et al. [9] Explored the use of computed tomography perfusion imaging (CTPI) in early diagnosis of acute RILI. They compared the CTPI values at pre- and post-radiation time points to measure the mean values of relative regional blood flow, relative regional volume, and relative regional permeability surface.

To overcome the limitations of known methods; e.g., the lack of PFTs to provide regional functionality, low spatial resolution of Nuclear imaging, and sensitivity to noise of conventional voxel-wise descriptors; we propose an efficient computational framework to accurately segment and align lung regions from the 4D-CT images; extract discriminative features and performs classification using deep a 3D convolutional neural network (CNN) to detect the RILI.

2. METHODS

The proposed framework, Fig. 2, performs sequentially: 4D lung segmentation; deformable image registration (DIR) for the 4D lung data, with a newly developed image models and methodology; extracts tex-

*Corresponding author, e-mail: aselba01@louisville.edu.

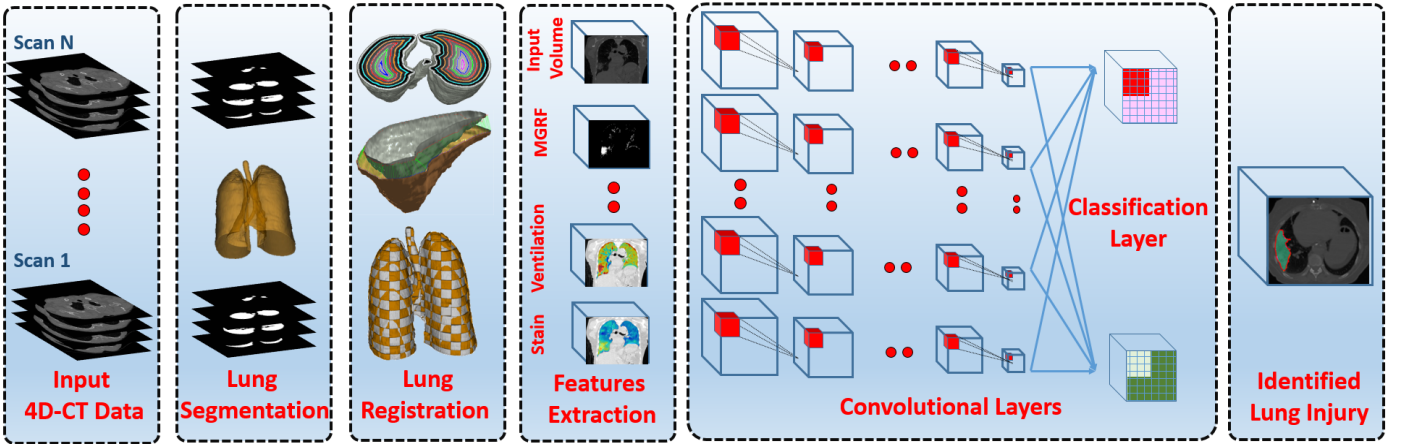


Fig. 2. Our framework for detecting the radiation-induced lung injuries (RILI).

tural and functional features, and detects the RILI by using a trainable deep CNN of lung tissues. Unlike our previous work [10, 11], this framework presents a new 4D-CT segmentation and registration techniques in addition to the deep 3D CNN for the identification of lung injury. The details of each step are given below.

2.1. 4D-CT Lung Segmentation

The segmentation of the lung fields is a crucial step for any computer aided diagnostic system (CAD) [12–15], and for all subsequent steps of our framework for many reasons. First, the lung fields are segmented in order to ensure that all potentially injured regions will be examined. Secondly, determination of the lung fields in CT scans reduces inter-subject variations of estimated features, which is achieved by normalizing the features inside the lung fields in each data set by averaging over its chest region. Thirdly, the segmented lung masks at different respiratory phases will be used for the deformable image registration (DIR). Finally, lung masks will be used as a volume of interest (VOI) for the analysis of the 3D CNN. Therefore, accurate segmentation is a must for accurate results at each step. We used our 3D lung segmentation framework [16] that is based on combining the segmentations of joint 3D Markov-Gibbs random field (MGRF) models for the original 3D scan and its Gaussian scale spaced-filtered volumes. The joint model integrates voxel-wise visual appearance features, pairwise spatial voxel interactions, and an adaptive shape prior of the lung that accounts for voxel location in addition to its intensity.

In order to segment the lung at different phases of the respiratory cycle, our method [16] is modified to increase its capability to segment 4D-CT data as follows: First, the exhale phase of the 4D data is segmented. Then, the segmentation labels of the the exhale volume are propagated to the subsequent respiratory phases using only the modified adaptive shape prior component, which leads to a an accurate and faster segmentation. Label propagation is based on the visual appearance of the CT images at the different respiratory phases. Namely, each voxel \mathbf{r} of the different phase image \mathbf{t} is mapped to the same location at the exhale lattice. Then, an initial search cube \mathbf{C}_r of size $c_{x:i} \times c_{y:i} \times c_{z:i}$ is centered at the mapped location \mathbf{r} for finding in the cube all the exhale voxels with signal deviations within a predefined fixed range, λ , from the mapped input signal, t_r . If such voxels are absent in the exhale, the cube size increases iteratively until the voxels within the predefined signal deviation range are found or the final cube size is reached ($c_{x:i} = c_{y:i} = c_{z:i} = 3$; λ from 50 to 125 with the step of $\Delta_\lambda = 25$, and the final cube size of $c_{x:f} = c_{y:f} = c_{z:f} = 11$ were used in our experiments). Then the voxel-wise probabilities, $P_{\text{shr}}(k)$; $k \in \mathbf{K}$, for the adaptive shape prior are estimated based on the found voxels of similar appearance and their labels. Let

$\mathbb{R}_r = \{\varphi : \varphi \in \mathbf{R}; \varphi \in \mathbf{C}_r; |g_\varphi - t_r| \leq \lambda\}$ be a subset of similar voxels within the cube \mathbf{C}_r in the exhale image. Let $R_r = \text{card}(\mathbb{R}_r)$ denote the cardinality (number of voxels) of this subset; and $\delta(z)$ be the Kronecker's delta-function: $\delta(0) = 1$ and 0 otherwise. The final probability for each voxel is calculated as: $P_{\text{shr}}(k) = \frac{1}{R_r} \sum_{\varphi \in \mathbb{R}_r} \delta(k - m_\varphi)$

2.2. Deformable Image Registration

Accurate estimation of regional functional features requires accurate spatial mapping between successive pairs of 3D CT volumes of the respiratory cycle. Traditional 4D-CT registration tries to establish direct spatial correspondences between the peak exhale and peak inhale images. However, this may lead to losing some accuracy that can be avoided due to relatively large changes in lung volumes between the two peak phases. To reduce these errors that can affect the estimated features, a sequential DIR has been performed between successive 3D-CT volumes of the respiratory cycle. The registration establishes the voxel-wise displacement vector field $\mathbf{U} = \{\mathbf{u}(\mathbf{r}) = \sum_{i=1}^{N-1} \mathbf{u}_i(\mathbf{r}) : \mathbf{r} \in \mathbb{R}\}$, which integrates displacements between successive 3D-CT volumes. The total field, \mathbf{U} , and its successive components, $\mathbf{U}_i = \{\mathbf{u}_i(\mathbf{r}) : \mathbf{r} \in \mathbb{R}\}$, defined on the initial 3D-CT volume \mathbb{R} , determine gradual changes of image geometry and signals or features along the cycle. We used our developed non-rigid registration technique [17] to get the displacement fields. This is achieved using a two-step registration, which includes a global affine step of the calculated distance map for the segmented lungs followed by a local deformation of each voxel to its correspondence by solving the 3D Laplace equation, $\nabla^2 \gamma = \frac{\partial^2 \gamma}{\partial x^2} + \frac{\partial^2 \gamma}{\partial y^2} + \frac{\partial^2 \gamma}{\partial z^2} = 0$; where $\gamma(x, y, z)$ is the estimated electric field between the reference and target surfaces, between each two corresponding iso-surfaces that generates streamlines from the fixed volume voxels to the moving one. Then, the generalized Gaussian Markov random field (GGMRF) smoothing is applied to ensure anatomical consistency and best match using Eq. 1

$$\begin{aligned} \widehat{\mathbf{p}}_s = \arg \min_{\widetilde{\mathbf{p}}_s = (\widetilde{x}_s^{ref}, \widetilde{y}_s^{ref}, \widetilde{z}_s^{ref})} & \left\{ \left(|x_s^{ref} - \widetilde{x}_s^{ref}|^\alpha + |y_s^{ref} - \widetilde{y}_s^{ref}|^\alpha + |z_s^{ref} - \widetilde{z}_s^{ref}|^\alpha \right) + \rho^\alpha \lambda^\beta \sum_{r \in N} \eta_{s,r} \right. \\ & \left. \left(|\widetilde{x}_s^{ref} - x_r^{ref}|^\beta + |\widetilde{y}_s^{ref} - y_r^{ref}|^\beta + |\widetilde{z}_s^{ref} - z_r^{ref}|^\beta \right) \right. \\ & \left. + |q_s^{tar} - \widetilde{q}_s^{ref}|^\alpha + \rho^\alpha \lambda^\beta \sum_{r \in N} \eta_{s,r} |\widetilde{q}_s^{tar} - q_r^{ref}|^\beta \right\} \quad (1) \end{aligned}$$

where $\mathbf{p}_s = (x_s^{ref}, y_s^{ref}, z_s^{ref})$ and $\widetilde{\mathbf{p}}_s = (\widetilde{x}_s^{ref}, \widetilde{y}_s^{ref}, \widetilde{z}_s^{ref})$ denote the initial 3D locations of the target voxels' correspondences and

their expected estimates on the reference; q_s^{tar} and \tilde{q}_s^{ref} are the target voxel intensity and its estimate correspondences on the reference, respectively; N is the number of the nearest neighbor voxels; $\eta_{s,r}$ is the GGMRF potential, and ρ and λ are scaling factors. The level of smoothing is controlled by the $\beta \in [1.01, 2.0]$ parameter (e.g., $\beta = 1.01$ for relatively abrupt vs. $\beta = 2$ for smooth edges). The prior distribution of the estimator is determined by $\alpha \in \{1, 2\}$ parameter. $\alpha = 2$ for Gaussian, or $\alpha = 1$ for Laplace. The used parameter values are $\rho = 1$, $\lambda = 5$, $\beta = 1.01$, $\alpha = 2$, and $\eta_{s,r} = \sqrt{2}$ for all directions.

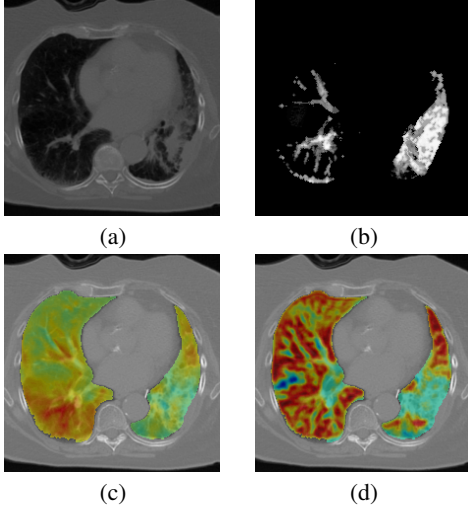


Fig. 3. A 2D axial slice (a) with its calculated 7th-order Gibbs energy (b), the maximal strain feature (c), and the Jacobian ventilation (d).

2.3. Extraction of Texture and Functionality Features

Two categories of discriminative features are extracted using the segmented lung volumes and the calculated deformation fields. These features describe the lung alteration as a result of the RT. The textural feature is modeled in terms of Gibbs energy for the novel 7th-order contrast-offset-invariant MGRF image model, while the functional features are modeled using the Jacobian ventilation, describing the air flow in the lung, and functional strain describing the elasticity of the lung tissue. Both of the feature categories are detailed below.

2.3.1. The 7th-order textural feature

To model the changes in visual appearance of the injured parts of the lung, the CT lung voxels are considered samples of a trainable translation- and contrast-offset-invariant 7th-order MGRF [18, 19]. The model relates the Gibbs probability of an image $\mathbf{g} = (g(\mathbf{r}) : \mathbf{r} \in \mathbb{R})$ with the voxel-wise HU $g(\mathbf{r})$ to a general-case 7th-order exponential family distribution: $P_7(\mathbf{g}) = \frac{1}{Z} \psi(\mathbf{g}) \exp(-E_7(\mathbf{g}))$; where Z is the normalizing factor and $E_7(\mathbf{g})$ is the Gibbs energy of the image. It describes an image texture in terms of signal dependencies (interactions) between each voxel and its neighbors depending on how the training lungs have been affected. This model accounts for partial ordinal interactions between voxel-wise signals in each particular voxel and within a radius ρ from it for describing the appearance of the injured parts in the lung CT scans. Given a training image \mathbf{g}° , Gibbs potentials, $v_{7;\rho}(g(\mathbf{r}')) : \mathbf{r}' \in \nu(\mathbf{r})$, of translation-invariant subsets of seven pixels to compute the energy $E_7(\mathbf{g})$ are learned using their approximate maximum likelihood estimates. The latter are obtained by generalizing the analytical approximation of potentials for the general 2nd-order MGRF in [20, 21]:

$$v_{7;\rho}(\beta) = \frac{F_{7;\rho;\text{core}}(\beta) - F_{7;\rho}(\beta|\mathbf{g}^\circ)}{F_{7;\rho;\text{core}}(\beta)(1 - F_{7;\rho;\text{core}}(\beta))}; \beta \in \mathbb{B}_7$$

where β denotes a numerical code of a particular contrast-offset invariant relation between seven signals; \mathbb{B}_7 is a set of these codes for

all these 7-signal co-occurrences; $F_{7;\rho}(\mathbf{g}^\circ)$ is a marginal probability of the code β ; $\beta \in \mathbb{B}_7$, over all the 7-voxel configurations with the radius ρ in the image \mathbf{g}° , and $F_{7;\rho;\text{core}}(\beta)$ is the like probability for the core distribution. The computed energy monitors changes in the tissue signals over time and indicates the RILI development. The computed energy gives an indication of the tissue signals changes over time and the possibility of lung injury development. While a severe radiation effect is suggested by the higher energy, the lower the Gibbs energy, the lower the injury. To quantify the normal and injured regions' appearances, we use the Gibbs energies for the three 7th-order contrast/offset- and translation-invariant MGRFs, each with a single family of central-symmetric, fixed-shape voxel configurations $\nu(\mathbf{r} = (x, y, z)) = \{(x, y, z); (x \pm \rho, y, z), (x, y \pm \rho, z), (x, y, z \pm \rho)\}$. Their distances, ρ , between the peripheral and central voxels and potentials are learned from \mathbf{g}° by modifying the learning process in [18].

2.3.2. Functionality features extraction

These groups of features are extracted from the calculated voxel-wise deformation fields obtained After the registration of successive respiratory phases, the obtained voxel-wise deformation fields are used to calculate the following functionality features:-

Functional Strain can be used for the identification of injured lung regions as the characteristics of these regions change as a result of the applied RT. The strain describes the elasticity characteristic of the lung tissues. From the gradient of the displacement vector $\mathbf{u}(\mathbf{r})$, which maps the voxel at location \mathbf{r} of the peak-exhale to its corresponding peak-inhale image, the Lagrangian strain can be estimated mathematically as follows:

$$S = \begin{bmatrix} \frac{\partial u_x}{\partial x} & \frac{1}{2} \left(\frac{\partial u_x}{\partial y} + \frac{\partial u_y}{\partial x} \right) & \frac{1}{2} \left(\frac{\partial u_x}{\partial z} + \frac{\partial u_z}{\partial x} \right) \\ \frac{1}{2} \left(\frac{\partial u_y}{\partial x} + \frac{\partial u_x}{\partial y} \right) & \frac{\partial u_y}{\partial y} & \frac{1}{2} \left(\frac{\partial u_y}{\partial z} + \frac{\partial u_z}{\partial y} \right) \\ \frac{1}{2} \left(\frac{\partial u_z}{\partial x} + \frac{\partial u_x}{\partial z} \right) & \frac{1}{2} \left(\frac{\partial u_z}{\partial y} + \frac{\partial u_y}{\partial z} \right) & \frac{\partial u_z}{\partial z} \end{bmatrix} \quad (2)$$

where the main diagonal components, $\frac{\partial u_x}{\partial x}$, $\frac{\partial u_y}{\partial y}$, and $\frac{\partial u_z}{\partial z}$ defines the linear strain along x , y , and z respectively. The shear strain components are calculated using the off-diagonal components as: $(\gamma_{ij} = \frac{1}{2} \left(\frac{\partial u_i}{\partial j} + \frac{\partial u_j}{\partial i} \right) = \gamma_{ji}; i, j \in \{x, y, z\}, i \neq j)$. In terms of $\mathbf{u}(\mathbf{r})$, the strain tensor can be expressed as: $S = \frac{1}{2} [\nabla \mathbf{u} + (\nabla \mathbf{u})^T]$, where:

$$\nabla \mathbf{u}(\mathbf{r}) = \begin{bmatrix} \frac{\partial u_x}{\partial x} & \frac{\partial u_x}{\partial y} & \frac{\partial u_x}{\partial z} \\ \frac{\partial u_y}{\partial x} & \frac{\partial u_y}{\partial y} & \frac{\partial u_y}{\partial z} \\ \frac{\partial u_z}{\partial x} & \frac{\partial u_z}{\partial y} & \frac{\partial u_z}{\partial z} \end{bmatrix} \quad (3)$$

Jacobian Ventilation, as the partial volume changes of the lung voxels give a good estimation of regional changes [5], incorporating this feature in terms of Jacobian ventilation will help in the detection of injured regions. The voxel-wise volume at the inhale phase is estimated as $V_{in}^r = V_{ex}^r J_r$ and the exhale-to-inhale volume change is $\Delta V_J = V_{in}^r - V_{ex}^r = V_{ex}^r (J_r - 1)$, where J_r is the Jacobian determinant for each voxel, estimated from the gradient of the displacement fields as $J_r = |\nabla \mathbf{u}(\mathbf{r}) + I|$, where I is the identity matrix, and $\nabla \mathbf{u}(\mathbf{r})$ is the gradient of $\mathbf{u}(\mathbf{r})$ for each voxel in Eq.(3).

2.4. Tissue Classification and Segmentation using Deep CNN

To detect and segment the injured tissues, all the estimated features ($E_7(\mathbf{g})$, ΔV_J , and the maximum eigenvalue of the strain matrix of Eq.(3)), in addition to the raw exhale phase (shown in Fig. 3) are used as 3D input volumes to the deep CNN. The latter learns discriminative characteristics from the different 3D inputs by using the training database containing both injured and normal lungs. A deep 3D CNN is used for the generation of soft segmentation maps followed by fully-connected 3D conditional random field (CRF) to produce the final labeled output of the segmented injuries [22]. The input is sequentially

convolved with multiple filters at the cascaded network layers. Each layer consists of a number of channels where each channel is corresponding to the 3D volume of the calculated feature. The 3D input feature volumes at the first layer are considered as the channels of the input, this process can be viewed as convolving 4D volumes (concatenated 3D feature volumes) with 4D kernels. The network architecture is depicted in Fig. 2. The architecture of the used CNN consists of seven layers with kernels of size 5^3 , the receptive field (Input voxel neighborhood influencing the activation of a neuron) size is 17^3 . The kernels for the classification layer is 1^3 . The advantage of this architecture is its ability to capture 3D contextual information from the provided feature volumes. The configuration parameters have been chosen heuristically similar to [22].

3. EXPERIMENTAL RESULTS AND CONCLUSION

4D-CT data from 13 lung cancer patients, scheduled to receive RT, has been used in this study. The 4D-CT data was collected using the Philips Brilliance Big Bore CT scanner with the Varian real-time position management (RPM) system (Varian Medical Systems, Palo Alto, CA) for respiratory traces. The data spacing for the collected data ranges from $1.17 \times 1.17 \times 2.0$ mm to $1.37 \times 1.37 \times 3.0$ mm. To obtain functionality and appearance features for training our CNN network, the CT data were contoured by a radiologist. Then the deep network was applied to the voxels within the VOI determined by the segmented lung mask in a “leave-one-subject-out scenario”. The voxels were classified as normal or injured tissue, and morphological operations were used for refinement, removal of scattered voxels, and hole filling. The 3D feature values, and the raw exhale volume (its HU values) inside the VOI are normalized to be zero mean and unity standard deviation to accelerate the convergence by reducing the internal covariant shift. Since lung segmentation and DIR are crucial steps in the proposed framework, Fig. 4 shows a 2D illustration of the 4D-CT segmentation that propagates the labels of the exhale phase to the inhale phase along the overlap between the two phase images before and after the DIR registration. The average lung segmentation accuracy in terms of Dice similarity coefficient (DSC) [23], which characterize spatial overlap, is 99% with average speed of 7.3 sec, while the DIR accuracy in terms of target registration error (TRE) equals 1.37 ± 1.03 mm. The perfor-

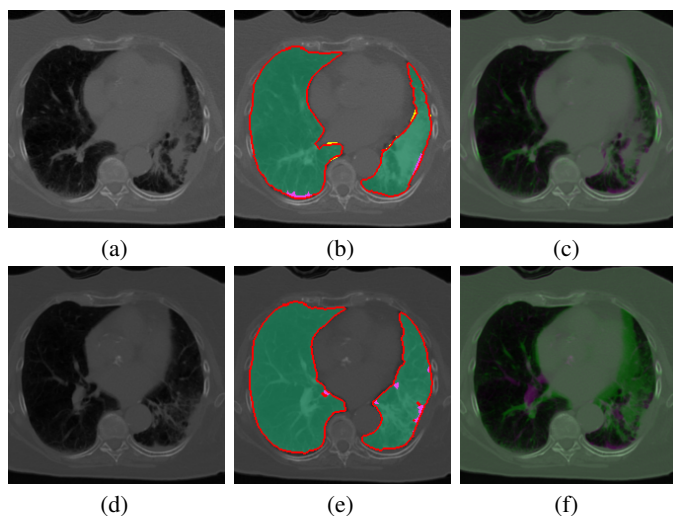


Fig. 4. A typical two axial slices at the same cross section for exhale phase (a) with its segmentation (d), and Inhale phase (b) with its segmentation (e) - their overlap before the registration (f) and after the registration (c). The color codes are: green for true positive, yellow for false positive, magenta for false negative, and red for ground truth edges.

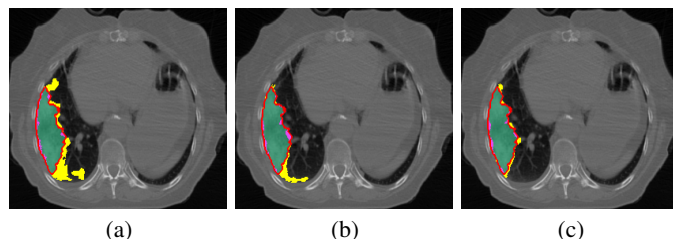


Fig. 5. A typical 2D segmentation results for one axial slice using FG1 (a), FG2 (b), and FG3 (c). The color codes are: green for true positive, yellow for false positive, magenta for false negative, and red for ground truth edges.

mance of the deep network tested on our datasets has been evaluated in terms of accuracy *Acc*, sensitivity *Sens*, and specificity *Spec*, defined as $Acc = \frac{TP+TN}{TP+TN+FP+FN}$, $Sens = \frac{TP}{TP+FN}$, $Spec = \frac{TN}{TN+FP}$ where *TP*, *TN*, *FP*, and *FN* are the number of true positive, true negative, false positive, and false negative respectively. The performance measures are listed in Table 1, for different feature group (FG), using only the raw exhale phase (FG1), exhale phase in addition to functionality features (FG2), and FG2 in addition to texture features (FG3). It is clear that combining the features achieves the highest accuracy because these features complement each other in both early and late phases.

Table 1. Performance of the 3D CNN for different feature groups: FG1 (4D-CT volume), FG2 (4D-CT volume and functionality features), and FG3 (4D-CT volume, functionality, and appearance features).

	Performance Metrics						
	Classification Metrics				Segmentation Metrics		
	AUC	Acc	Sens	Spec	Dice	BHD	AVD
FG1	94.1	91.8	79.1	96.3	72.7	19.4	9.5
FG2	96.3	92.6	81.0	96.5	82.9	14.2	6.0
FG3	99.0	95.4	86.8	98.3	88.0	5.2	4.6

Moreover, the classification accuracy has been evaluated using the area under the curve (AUC) for different feature groups. The AUC for using the FG1 only equals 0.94, while for the FG2 equals 0.96. When combining all the features in the classification process, the AUC has increased to 0.99. This enhancement highlights the advantages of integrating both the texture and functionality features as discriminatory ones for the detection of RILI.

In addition to the DSC, the segmentation accuracy for the injured tissues has been evaluated for each subject with bidirectional Hausdorff distance (BHD), and percentage volume difference (PVD) [24, 25], which characterize maximum surface-to-surface distances, and volume differences, respectively, between the segmented and “ground-truth” injured regions. Table 1 summarizes the DSC, BHD, and PVD statistics for all test subjects showing the effect of different FG of our framework. The ground truth borders were outlined manually by a radiologist. The mean \pm standard deviation of the DSC, BHD, and PVD for all the test subjects using our proposed framework is $88.0 \pm 3.5\%$, 5.2 ± 1.3 mm, and $4.6 \pm 0.7\%$, respectively. Figure 5 shows sample RILI segmentation using different FGs.

In conclusion, this paper introduced a processing pipeline for the detection of RILI using 4D-CT lung data. The pipeline consists of 4D-CT lung segmentation, deformable image registration, extraction of discriminative feature, and injured tissue segmentation using 3D CNN. The segmentation/detection results on a set of 13 patients who underwent the RT confirm that the proposed framework holds the promise for early detection for lung injury. We plan to integrate other clinical biomarkers, e.g., PFTs, to our framework, and perform a more validation by collecting more data with shorter follow-up scans to evaluate the ability of detecting the RILI before any radiographical evidence.

Acknowledgment: This research work has been supported by Research Grant from the Kentucky Lung Cancer Research Program.

4. REFERENCES

- [1] A. R. Larici, A. del Ciello, F. Maggi, S. I. Santoro, B. Meduri, V. Valentini, A. Giordano, and L. Bonomo, "Lung abnormalities at multimodality imaging after radiation therapy for non-small cell lung cancer," *Radiographics*, vol. 31, no. 3, pp. 771–789, 2011.
- [2] P. Giridhar, S. Mallick, G. K. Rath, and P. K. Julka, "Radiation induced lung injury: prediction, assessment and management," *Asian Pac J Cancer Prev*, vol. 16, no. 7, pp. 2613–2617, 2015.
- [3] M. Negahdar, N. Dunlap, A. Zacarias, A. C. Civelek, S. Y. Woo, and A. A. Amini, "Comparison of indices of regional lung function from 4-D X-ray CT: jacobian vs. strain of deformation," in *2013 IEEE 10th International Symposium on Biomedical Imaging*. IEEE, 2013, pp. 648–651.
- [4] K. Latifi, T. Dilling, S. Hoffe, C. Stevens, E. Moros, and G. Zhang, "SU-E-J-187: evaluation of the effects of dose on 4DCT-Calculated lung ventilation," *Medical Physics*, vol. 39, no. 6, pp. 3695–3696, 2012.
- [5] J. M. Reinhardt, K. Ding, K. Cao, G. E. Christensen, E. A. Hoffman, and S. V. Bodas, "Registration-based estimates of local lung tissue expansion compared to xenon ct measures of specific ventilation," *Medical image analysis*, vol. 12, no. 6, pp. 752–763, 2008.
- [6] A. R. Cunliffe, S. G. Armato III, C. Straus, R. Malik, and H. A. Al-Hallaq, "Lung texture in serial thoracic CT scans: correlation with radiologist-defined severity of acute changes following radiation therapy," *Physics in medicine and biology*, vol. 59, no. 18, pp. 5387, 2014.
- [7] Y. Vinogradskiy, L. Schubert, D. Brennan, R. Castillo, E. Castillo, T. Guerrero, M. Miften, B. Kavanagh, and M. Mary, "Clinical validation of 4DCT-Ventilation with pulmonary function test data," *International Journal of Radiation Oncology Biology Physics*, vol. 90, no. 1, pp. S61–S62, 2014.
- [8] H. Sharifi, W. Van Elmpt, C. Oberije, G. Nalbantov, M. Das, M. Öllers, P. Lambin, A.-M. C. Dingmans, and D. De Ruyscher, "Quantification of CT-assessed radiation-induced lung damage in lung cancer patients treated with or without chemotherapy and cetuximab," *Acta Oncologica*, vol. 55, no. 2, pp. 156–162, 2016.
- [9] X.-Y. Hu, X.-M. Fang, H.-W. Chen, X.-J. Yao, P.-Y. Qian, J.-Y. Zhou, J. Guo, A. Lerner, and C.-H. Hu, "Early detection of acute radiation-induced lung injury with multi-section CT perfusion imaging: An initial experience," *Clinical radiology*, vol. 69, no. 8, pp. 853–860, 2014.
- [10] A. Soliman, F. Khalifa, A. Shaffie, N. Liu, N. Dunlap, B. Wang, A. Elmaghraby, G. Gimel'farb, and A. El-Baz, "Image-based cad system for accurate identification of lung injury," in *Image Processing (ICIP), 2016 IEEE International Conference on*. IEEE, 2016, pp. 121–125.
- [11] A. Soliman, F. Khalifa, A. Shaffie, N. Dunlap, B. Wang, A. Elmaghraby, and A. El-Baz, "Detection of lung injury using 4D-CT chest images," in *2016 IEEE 13th International Symposium on Biomedical Imaging (ISBI)*. IEEE, 2016, pp. 1274–1277.
- [12] A. El-Baz, G. M. Beache, G. Gimel'farb, K. Suzuki, K. Okada, A. Elnakib, A. Soliman, and B. Abdollahi, "Computer-aided diagnosis systems for lung cancer: challenges and methodologies," *International journal of biomedical imaging*, vol. 2013, 2013.
- [13] A. Soliman, A. Elnakib, F. Khalifa, M. A. El-Ghar, and A. El-Baz, "Segmentation of pathological lungs from CT chest images," in *2015 IEEE International Conference on Image Processing (ICIP)*. IEEE, 2015, pp. 3655–3659.
- [14] A. Soliman, F. Khalifa, A. Alansary, G. Gimel'farb, and A. El-Baz, "Segmentation of lung region based on using parallel implementation of joint MGRF: validation on 3D realistic lung phantoms," in *2013 IEEE 10th International Symposium on Biomedical Imaging (ISBI)*. IEEE, 2013, pp. 864–867.
- [15] B. Abdollahi, A. Soliman, A. Civelek, X.-F. Li, G. Gimelfarb, and A. El-Baz, "A novel 3D joint MGRF framework for precise lung segmentation," in *International Workshop on Machine Learning in Medical Imaging*. Springer, 2012, pp. 86–93.
- [16] A. Soliman, F. Khalifa, A. Elnakib, M. A. El-Ghar, N. Dunlap, B. Wang, G. Gimel'farb, R. Keynton, and A. El-Baz, "Accurate lungs segmentation on CT chest images by adaptive appearance-guided shape modeling," *IEEE Transactions on Medical Imaging*, 2016.
- [17] A. Soliman, F. Khalifa, N. Dunlap, B. Wang, M. A. El-Ghar, and A. El-Baz, "An iso-surfaces based local deformation handling framework of lung tissues," in *2016 IEEE 13th International Symposium on Biomedical Imaging (ISBI)*. IEEE, 2016, pp. 1253–1259.
- [18] N. Liu, G. Gimel'farb, and P. Delmas, "High-order MGRF models for contrast/offset invariant texture retrieval," in *Proc. Int. Conf. Image Vision Computing New Zealand*. 2014, pp. 96–101, ACM.
- [19] N. Liu, A. Soliman, G. Gimelfarb, and A. El-Baz, "Segmenting kidney DCE-MRI using 1st-order shape and 5th-Order appearance priors," in *International Conference on Medical Image Computing and Computer-Assisted Intervention*. Springer, 2015, pp. 77–84.
- [20] G. Gimel'Farb and A. Farag, "Texture analysis by accurate identification of simple markovian models," *Cybernetics and Systems Analysis*, vol. 41, no. 1, pp. 27–38, 2005.
- [21] A. El-Baz, G. Gimelfarb, and J. S. Suri, *Stochastic modeling for medical image analysis*, CRC Press, 2015.
- [22] K. Kamnitsas, C. Ledig, V. F. Newcombe, J. P. Simpson, A. D. Kane, D. K. Menon, D. Rueckert, and B. Glocker, "Efficient multi-scale 3D CNN with fully connected CRF for accurate brain lesion segmentation," *arXiv preprint arXiv:1603.05959*, 2016.
- [23] K. H. Zou, S. K. Warfield, A. Bharatha, C. M. C. Tempany, M. R. Kaus, S. J. Haker, W. M. Wells III, F. A. Jolesz, and R. Kikinis, "Statistical validation of image segmentation quality based on a spatial overlap index," *Academic Radiology*, vol. 11, no. 2, pp. 178–189, 2004.
- [24] G. Gerig, M. Jomier, and M. Chakos, "Valmet: A new validation tool for assessing and improving 3D object segmentation," in *International Conference on Medical Image Computing and Computer-Assisted Intervention*. Springer, 2001, pp. 516–523.
- [25] A. Soliman, F. Khalifa, A. Alansary, G. Gimel'farb, A. El-Baz, C. Sun, T. Bednarz, T. D. Pham, P. Vallotton, and D. Wang, "Performance evaluation of an automatic MGRF-based lung segmentation approach," in *AIP Conference Proceedings*. AIP, 2013, vol. 1559, pp. 323–332.